Analysis and Design of High-Frequency Converter With Resistive Matching Network and Spiral Inductor

Yueshi Guan, *Student Member, IEEE*, Qing Bian, Yijie Wang, *Senior Member, IEEE*, Xihong Hu, Bin Liu, Wei Wang, and Dianguo Xu, *Fellow, IEEE*

***Abstract*—In this paper, two resistive matching networks are proposed, which can maintain the resistive transferring property under different load conditions. The high-frequency converter based on the resistive network can adequately achieve the soft-switching characteristics within a large load variation range, which helps to reduce switching losses and improve system efficiency. At the same time, a detailed design method for planar spiral inductor is described. In addition, the quality factor characteristics of different winding structures are analyzed. A 20-MHz high-frequency dc/dc converter based on the T-type matching network and circular spiral inductor is designed in this paper. The experimental results verify the advantages of the proposed resistive matching network and spiral inductor.**

***Index Terms*—DC/DC converter, high frequency, resistive matching network, spiral Inductor.**

I. Introduction

INCREASING demand of high power density has been put forward in power electronics systems. The most effective way to achieve a high-power-density power converter is to increase the switching frequency [1]–[6]. At high operating frequencies, the energy stored in capacitors and inductors during each operating period can be significantly reduced, which helps to decrease their values and volumes. Usually these passive components take most of the system volume and weight. Meanwhile, high operating frequency can help systems achieve fast dynamic response. Thus, high-frequency power electronic technology has become a research subject of interest. Many high-frequency converters have been adopted in LED drivers, computer adaptors, cubesat plasma thruster, and other weight or volume critical application fields [7]–[9].

However, despite these merits, many problems need to be addressed as the switching frequency increasing above tens of megahertz. One critical challenge is high switching losses, which form a proportional relationship with the switching frequency. The most common method for reducing the switching losses is to adopt a resonant converter with good soft-switching characteristics, such as the quasi-resonant converter (QRC) and multiresonant converter (MRC) [10]–[12]. Among these resonant converters, the half-bridge structure is not suitable for operating in tens of megahertz frequency condition because the small dead time of the driving signal is highly difficult to control and the driving circuit is more complex than that of a single-switch converter topology with the switch connected to ground.

Many single-switch high-frequency topologies have been proposed and researched, including the resonant SEPIC converter, and Class Φ_2 converter [13]–[17]. In general, these single-switch high-frequency converters consist of three stages: the inverter stage, the impedance transformation stage, and the rectifier stage [18]–[20]. Among these topologies, the parasitic capacitance and inductance are absorbed into the circuit to achieve resonant soft-switching transitions in inverter and rectifier stage. Usually, an impedance transformation stage is added between the inverter stage and the rectifier stage to achieve the desired output power by adjusting the equivalent resistance of rectifier stage. The impedance transformation stage can be realized by an isolation transformer or nonisolation matching network composed of inductors and capacitors. The matching network can transform the impedance only within a narrow band, and the transformer can effectively transform the impedance within a broad band by converting the voltage and current. However, for a transformer, the leakage inductance and parasitic capacitance in high-frequency condition are difficult to control. In addition, these parameters affect the operating modes of high-frequency converters. For matching networks, the L-type matching network is the most commonly adopted one, which can be built only by one capacitor and one inductor [21]–[23]. However, in L-type matching network, the soft-switching characteristics of switch lose with the variation of load. Thus, the switching losses increase and system efficiency decreases. So it is necessary to design a matching network that can help the switch operate in a good soft-switching condition within a wide load variation range.

In high-frequency condition, another highly important issue is magnetic components. When the switching frequency is in tens of megahertz, magnetic cores are not necessary for inductors and transformers with small values. Under nonisolation conditions, air core inductor can be adopted in high-frequency converters which eliminate core losses. There are various structures for air core inductors, such as spiral, solenoid, and toroid. Commercial air core inductors with inductance values between 1 nH to tens

Manuscript received March 30, 2017; revised June 5, 2017; accepted July 19, 2017. Date of publication July 31, 2017; date of current version February 22, 2018. This work was supported by the National Key Research and Development Program of China under Grant 2017YFB0402800. Recommended for publication by Associate Editor J. M. Rivas Davila. *(Corresponding author: Yijie Wang.)*

The authors are with the School of Electrical Engineering and Automation, Harbin Institute of Technology, Harbin 150001, China (e-mail: hitguanyueshi@sina.com; 959411403@qq.com; wangyijie@hit.edu.cn; 15754602978@163.com; liubin15s@163.com; wangwei602@hit.edu.cn; xudiang@hit.edu.cn).

Color versions of one or more of the figures in this paper are available online at http://ieeexplore.ieee.org

Digital Object Identifier 10.1109/TPEL.2017.2734107

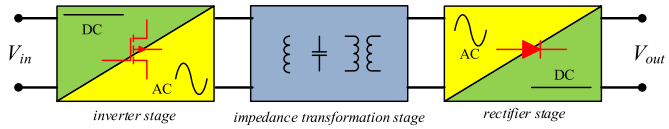

Fig. 1. Block diagram of typical high-frequency single-switch converters.

of microhenry are available in high-frequency condition, such as the Spring series from Coilcraft, some typical values can be obtained, and the structure of these inductors is the solenoid [24]. Another air core inductor structure is the spiral, with only PCB traces and FR4 material, which has been adopted in some high-frequency converters [25]–[27]. On the basis of the copper tracks on a PCB, the inductances can be flexibly adjusted during the design process. Some effective equations and tools can help to design planar spiral inductors [28]–[31]. For example, the expressions for planar spiral inductances with four typical winding structures are described in [31]. Meanwhile, although there are no core losses, in high-frequency condition, the copper losses caused by resistance significantly increase. Thus, it is necessary to analyze the quality factor characteristics of different winding structures.

In this paper, a 20-MHz high-frequency dc/dc converter based on a T-type matching network and a spiral inductor is presented. In Section II, the analysis of the phase characteristics for three different matching networks is described, and the resistive transferring characteristics of the T-type and π-type matching network is described. In Section III, an analysis of the effects of impedance amplitude and the rectifier phase is discussed. In Section IV, the derivation procedure of spiral inductor with circular and square windings is introduced. In addition, the quality factor characteristics of different winding structures are compared. In Section V, a 10-W prototype is built, where the input voltage is 8 V and the output voltage is 5 V. The control method and experimental results are described in detail. The conclusion is provided in Section VI.

II. Analysis of Matching Networks

Fig. 1 shows a typical block diagram of high-frequency converters based on single-switch structure, which consists of three stages: the inverter stage, the impedance transformation stage, and the rectifier stage. The inverter stage converts the dc voltage to high-frequency ac voltage. The switch in the inverter stage is expected and designed to operate in the ZVS condition on the basis of the resonance of the inductor and the capacitor. The rectifier stage regulates the ac voltage to dc voltage based on diode operating in the resonant situation. To reduce reactive power losses, the rectifier stage is usually designed to be resistive. Typically, in-phase fundamental rectifier voltage and current correspond to the best converter operating efficiency. This is not surprising as it minimizes the circulating currents for a given level of output power. Meanwhile, to achieve the desired the output power, an impedance transformation stage is usually added between the inverter and rectifier stages, which can adjust the drain-source impedance by transferring the equivalent resistance of rectifier stage. The matching network is usually composed of capacitors and inductors. In the following discussion, a detailed analysis of different matching networks is presented.

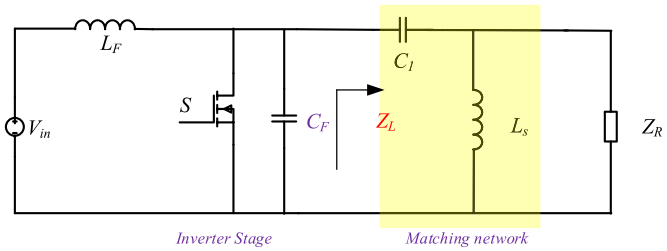

Fig. 2. High-frequency resonant SEPIC converter in [23].

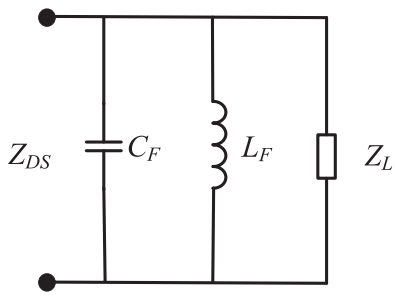

Fig. 3. Impedance diagram when the switch turns off.

A. L-type Matching Network

Fig. 2 shows the circuit of the high-frequency resonant SEPIC converter where rectifier stage is represented by the equivalent resistor Z_R. To achieve desired output power P_o, the output impedance of the inverter stage can be calculated to be $Z_L = V_{DS}^2/P_o$. The L-type high-pass matching network, composed of C_1 and L_s, as shown in the yellow region, is adopted here to transfer the equivalent resistance Z_R to a desired value Z_L. So at a certain operating frequency ω, the parameters C_1 and L_s can be calculated as

$$\begin{cases} L_s = \frac{Z_R}{\omega}\sqrt{\frac{Z_L}{Z_R - Z_L}} \\ C_1 = \frac{1}{\omega\sqrt{Z_L(Z_R - Z_L)}} \end{cases}. \tag{1}$$

From (1), it can be seen that the matching network in Fig. 2 is a high-pass low-to-high L-type matching network; here, Z_L has to be smaller than Z_R. When the switch turns off, the impedance Z_{DS} between the switch source and drain can be represented, as shown in Fig. 3, and the impedance Z_{DS} determines the switch drain-source voltage waveforms. The resonant frequency of the inverter stage can be calculated as

$$f_F = \frac{1}{2\pi\sqrt{L_F C_F}}. \tag{2}$$

However, with a change in equivalent resistance Z_R under different output power conditions, the transferred impedance Z_L can not remain resistive in the L-type matching network.

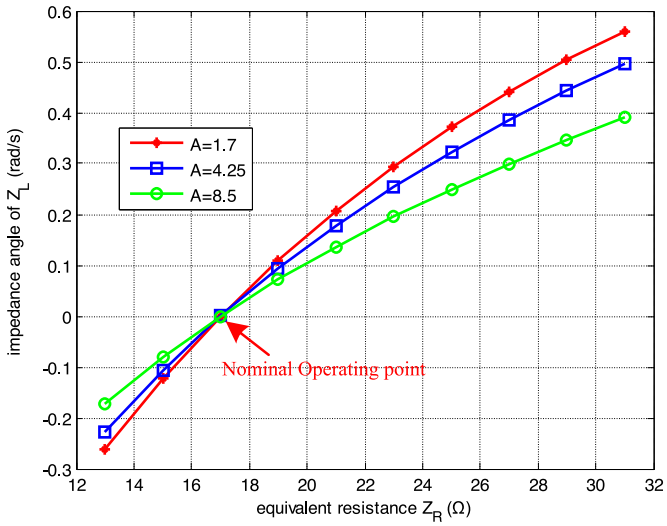

Fig. 4. Angle curve of impedance Z_L with change of Z_R in L-type matching network.

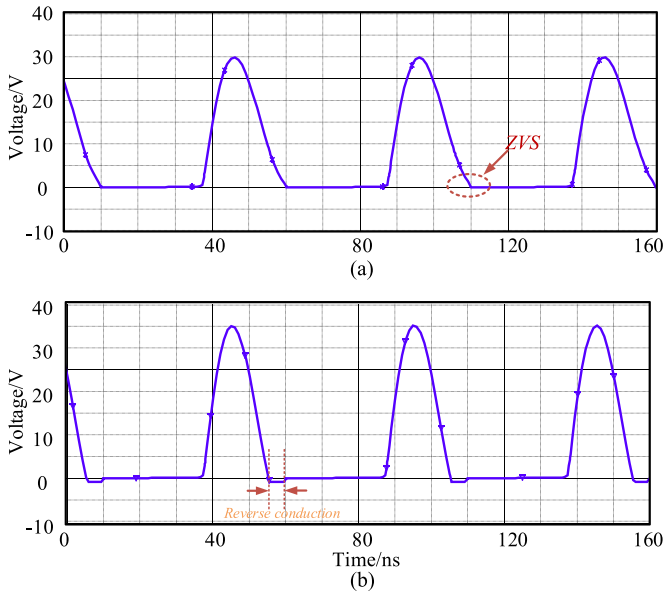

Fig. 5. Drain-source voltage waveforms under different equivalent load conditions. (a) $Z_R = 17\,\Omega$, (b) $Z_R = 34\,\Omega$.

The impedance angle of Z_L can be calculated as

$$\theta_{Z_L} = \arctan\left(\mathrm{Im}\left(Z_L\right)/\mathrm{Re}\left(Z_L\right)\right). \tag{3}$$

Fig. 4 shows the curve of θ_{Z_L} when the equivalent resistance Z_R changes. The parameter $A = Z_R/Z_L$ represents the transfer ratio at the nominal operating point, and at this point, the impedance Z_L is designed to be resistive, as shown in Fig. 4. It can be seen that with an increase in Z_R, the angle of Z_L becomes larger than zero, which means Z_L changes to be inductive. On the contrary, the impedance Z_L behaves capacitive. The nonresistive characteristics of Z_L induces extra inductance or capacitance components in the resonant tank, which affects the resonant frequency and operating characteristics of the high-frequency converter.

Fig. 5 shows the switch drain-source voltage of the high-frequency resonant SEPIC circuit shown in Fig. 2 under different Z_R conditions. Fig. 5(a) shows the waveform of v_{DS} at the nominal operating point. It can be seen that at the turn-on point the voltage v_{DS} just resonates to be zero which means the switch can achieve ZVS turn-on characteristics. However, as shown in Fig. 5(b), when the equivalent rectifier load Z_R doubles, the ZVS characteristics loss and the drain-source voltage is clamped by the reverse conduction of the switch body diode. The reverse conduction causes large reverse conduction losses in high-frequency condition. According to (2) and Fig. 4, it can be concluded that the resonant period decreases because of the extra inductive component of transferred impedance Z_L. Thus, to guarantee the switch operating in the soft-switching condition within a large load variation range, it is necessary to adopt and design matching networks with resistive transferring characteristics.

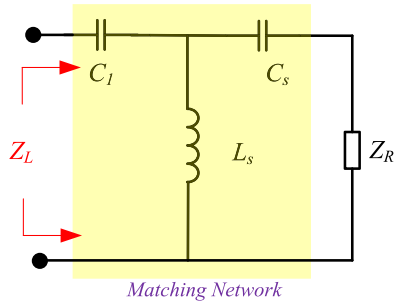

Fig. 6. Diagram of the T-type matching network.

B. T-type Matching Network

In the following discussion, a T-type matching network is adopted and analyzed to solve this problem. Fig. 6 shows a diagram of the T-type matching network, which is composed of two capacitors and one inductor.

In the frequency domain, the transferred impedance of the T-type matching network can be calculated as

$$Z_L = \frac{s^3 Z_R C_1 L_s C_s + s^2\left(L_s C_1 + L_s C_s\right) + s C_s Z_R + 1}{s^3 C_1 L_s C_s + s^2 C_1 C_s Z_R + s C_1}. \tag{4}$$

The basic requirement of the matching network is to guarantee the transferred impedance Z_L to be resistive at nominal operating angular frequency ω. Based on the earlier rule, in the numerator and denominator of (4), the coefficients of the imaginary and real components must be in proportion and satisfy

$$\frac{1-\omega^2\left(L_s C_1 + L_s C_s\right)}{-\omega^2 C_1 C_s Z_R} = \frac{C_s Z_R\left(1-\omega^2 C_1 L_s\right)}{C_1\left(1-\omega^2 L_s C_s\right)} = Z_L. \tag{5}$$

TABLE I
PARAMETERS IN DIFFERENT NOMINAL OPERATING CONDITIONS
($f = 20$ MHz)

Z_R	Z_L	k	C_s (pF)	C_1 (pF)	L_s (nH)
17	5	0.5	1977.7	988.85	77.38
17	5	1	863.14	863.14	73.37
17	5	1.3	560.44	728.57	76.05
17	5	1.5	398.32	597.48	83.91
17	10	0.5	1756.8	878.42	123.58
17	10	1	610.33	610.33	103.76
17	10	1.3	72.95	56.11	496.05

Here, $C_1 = kC_s$, then (6) and (7) can be obtained according to (5)

$$\omega^2 C_s L_s = \frac{Z_R - kZ_L}{k(Z_R - Z_L)} \tag{6}$$

$$Z_L Z_R = \frac{\omega^2 L_s C_s (k+1) - 1}{k\omega^2 C_s^2}. \tag{7}$$

Based on these equations, the final values of C_1, C_s, and L_s can be calculated as

$$\begin{cases} C_s = \frac{1}{\omega k}\sqrt{\frac{Z_L k^2 - Z_R}{Z_L Z_R (Z_L - Z_R)}} \\ C_1 = \frac{1}{\omega}\sqrt{\frac{Z_L k^2 - Z_R}{Z_L Z_R (Z_L - Z_R)}} \\ L_s = \frac{1}{\omega^2 C_s}\frac{Z_R - kZ_L}{k(Z_R - Z_L)} \end{cases}. \tag{8}$$

The T matching network can achieve two matching cases: one is the low-to-high case ($Z_L < Z_R$), and the other is the high-to-low case ($Z_L > Z_R$). Some insight guidance to understand these two cases can be seen from [32]. For these two different matching cases, the restrictions of k are quite different. For the low-to-high case, according to (6) to (8), (9) should be satisfied

$$\begin{cases} Z_R - Z_L > 0 \\ Z_R - kZ_L > 0 \\ Z_R - k^2 Z_L > 0 \end{cases}. \tag{9}$$

From (9), the variation range of k in the low-to-high matching case can be calculated as

$$0 < k < \sqrt{Z_R / Z_L}. \tag{10}$$

With a similar method, in the high-to-low matching case, the restrictions can be obtained as

$$\begin{cases} Z_R - Z_L < 0 \\ Z_R - kZ_L < 0 \\ Z_R - k^2 Z_L < 0 \end{cases}. \tag{11}$$

Based on (11), the variation range of k in the high-to-low matching case can be calculated as

$$\sqrt{Z_R / Z_L} < k. \tag{12}$$

Taking the low-to-high case as an example, in different k values and nominal operating conditions, the parameter values are calculated as shown in Table I. It can be seen that at the same transfer ratio $A = Z_R/Z_L$, with increasing k, the values of capacitors C_s and C_1 decrease. The minimum value of inductor L_s is achieved when $k = 1$. On the other hand, at the same k, with the decrease in transfer ratio A, the values of the two capacitors also decrease while the value of the inductor L_s increases.

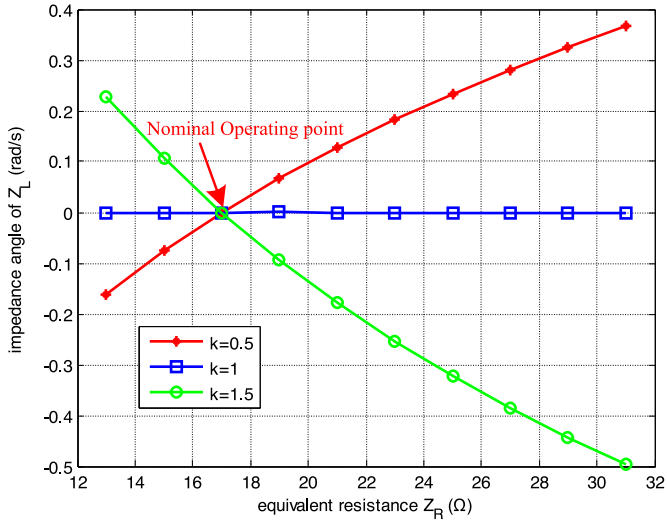

Fig. 7. Angle curves of impedance Z_L with change of Z_R in T-type matching network.

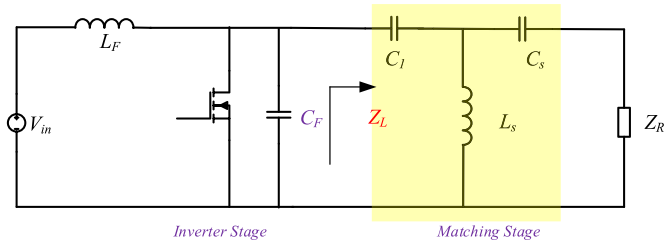

Fig. 8. High-frequency converter with T-type matching network.

From the preceding analysis and parameters at the nominal point, Fig. 7 shows the angle curve of impedance Z_L when the equivalent resistance Z_R changes. It can be seen that when k is smaller than 1, the impedance Z_L becomes inductive with the increment of impedance Z_R. The trend is similar to that of the L-type matching network. However, when k is larger than 1, the impedance Z_L becomes capacitive with the increment of impedance Z_R. The expected characteristics appears when $k = 1$. In this condition, the impedance angle of Z_L always remains zero, it means Z_L is resistive no matter how the equivalent resistance Z_R changes. The same conclusion can also be drawn after substituting the corresponding parameters into (4), where the imaginary parts are zero.

From the preceding analysis, Fig. 8 shows the circuit of a high-frequency converter with the T-type matching network at $k = 1$ which replaces the L-type matching network in the high-frequency resonant SEPIC converter. Fig. 9 shows the simulation results at $Z_R = 17\,\Omega$ and $Z_R = 34\,\Omega$ condition, respectively. From Fig. 9(a), it can be seen that the switch can turn on in the ZVS condition at the nominal operating point and the drain-source voltage waveform is the same as that in Fig. 5(a). Fig. 9(b) shows the voltage waveform when the equivalent

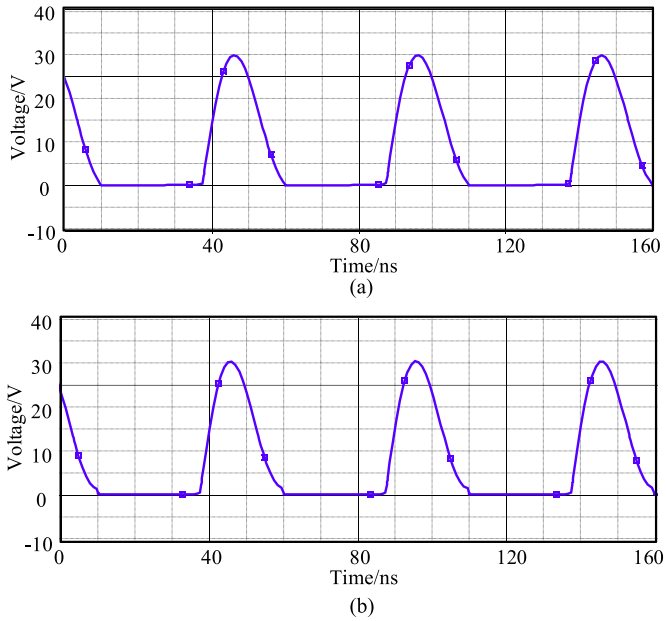

Fig. 9. Drain-source voltage waveforms of high-frequency converter with T-type matching network. (a) $Z_R = 17\,\Omega$, (b) $Z_R = 34\,\Omega$.

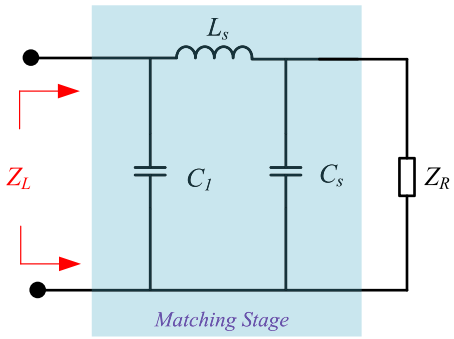

Fig. 10. π-Type matching network.

rectifier load Z_R doubles, the waveform is similar to that at the nominal operating point. Except at the turn-on point, the drain-source voltage is a little bit higher than zero, which is caused by the magnitude change of the transferred impedance Z_L, which will be analyzed in the next section. The resistive T-type matching network leads small changes to the resonant tank of inverter stage because of no extra inductive or capacitive components added. Comparing with the reverse conduction losses in L-type network, T-type matching network can guarantee well switching characteristics and small switching losses.

At the same time, because of the duality characteristics, a similar π-type matching network is also proposed, as shown in Fig. 10. With a similar design procedure to that for the T-type matching network, the parameter expressions of the π-type matching network can be obtained.

In addition, assuming $C_1 = kC_s$, Fig. 11 shows the angle curves of impedance Z_L when the equivalent resistance Z_R changes. Similar to the T-type matching network when $k = 1$, the impedance angle of Z_L always remains at zero, which means

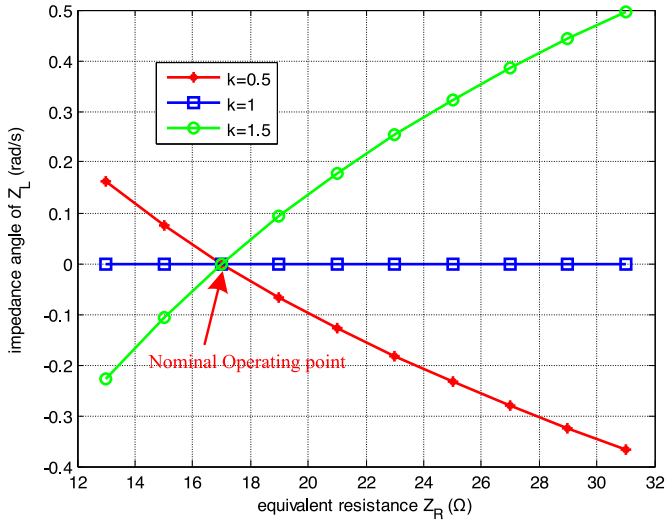

Fig. 11. Angle curves of impedance Z_L with change of Z_R in π-type matching network.

that Z_L is resistive, no matter how the equivalent resistance Z_R changes.

III. Effect Analysis of Impedance Amplitude and Rectifier Phase

Based on earlier analyses, it can be seen that for the L-type matching network, the soft-switching characteristics lose with the variation of rectifier equivalent impedance. Meanwhile, for the T-type or π-type matching network, when $k = 1$, the switch drain-source voltage is almost not affected by a change in rectifier equivalent impedance Z_R. In Section II, the phase transferring characteristics of different matching networks are analyzed. However, it cannot be solidly proven that the well operating property is caused by only the phase preservation of the T matching network, because the amplitude of impedance Z_L will also change and the equivalent impedance Z_R may not be always resistive. In the following section, these two points will be discussed.

A. Effect of Impedance Amplitude

In the preceding analysis, the most concern is that the phase change of impedance Z_L affects the operation mode of the resonant inverter. However, with the variation in Z_R, the amplitude of the transferred impedance Z_L will also change, which may also affect the operating condition of the inverter stage. In this part, the effect of impedance amplitude will be analyzed.

For the T-type matching network, Z_{T_L0} and Z_{T_R0} are defined as the impedance values at the nominal operating point. Taking $k = 1$, for example, for a constant operating frequency, the relationship between Z_{T_L} and Z_{T_R} in the T-type matching network can be calculated as

$$Z_{T\_L} = \frac{Z_{T\_L0} Z_{T\_R0}}{Z_{T\_R}}. \tag{13}$$

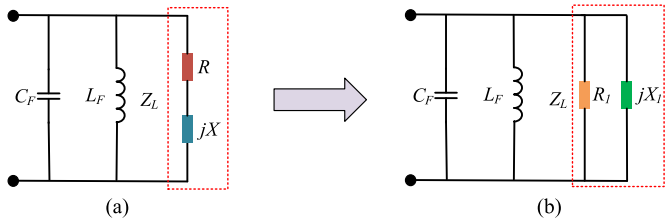

Fig. 12. Series and parallel structures of resistance and reactance in Z_L.

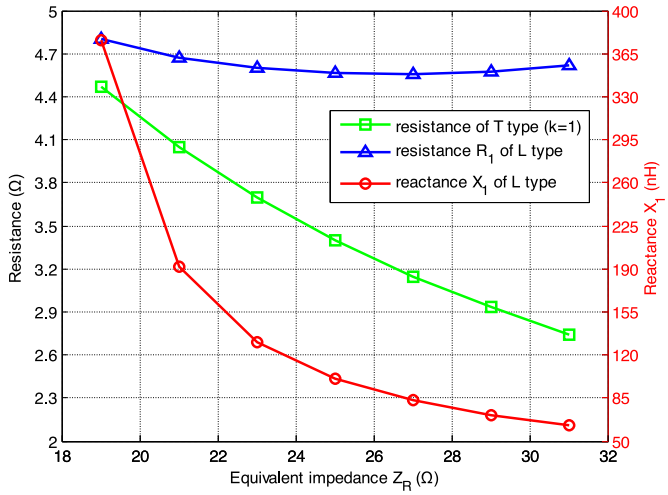

Fig. 13. Resistance and reactance curves of T-type ($k = 1$) and L-type matching networks.

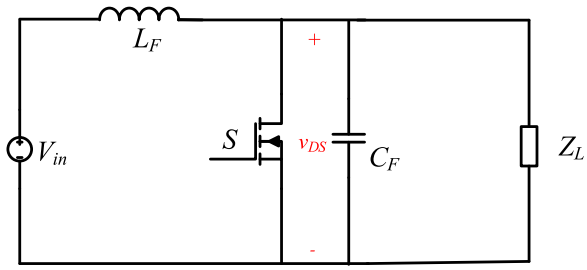

Fig. 14. Circuit of the simplified inverter stage with load Z_L.

It can be seen that impedance Z_{T_L} forms an inversely proportional relationship with Z_{T_R} and is always resistive. With a similar method, the relationship between Z_{L_L} and Z_{L_R} in the L-type matching network can be calculated as

$$Z_{L\_L} = R + jX = \frac{Z_{L\_R} Z_{L\_L0} Z_{L\_R0} A + j\left(Z_{L\_L0}\sqrt{A-1}\left(Z_{L\_R}^2 - Z_{L\_R0}^2\right)\right)}{Z_{L\_R0}^2 + Z_{L\_R}^2 (A-1)} \quad (14)$$

where Z_{L_L0} and Z_{L_R0} also represent the impedance values at the nominal operating point, and $A = Z_{L\_L0}/Z_{L\_R0}$. Meanwhile, the resistance part R and the reactance part X can be

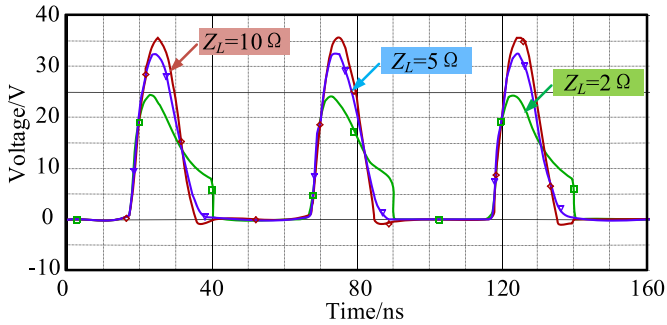

Fig. 15. Simulation results of switch drain-source voltages with different Z_L.

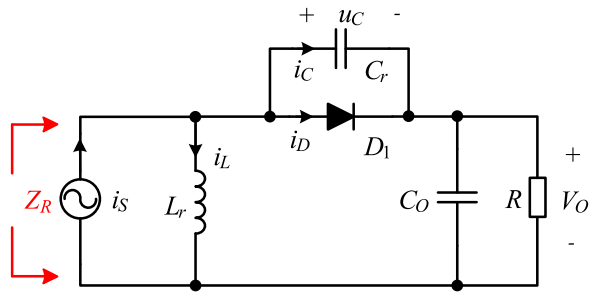

Fig. 16. Resonant rectifier adopted in the high-frequency converter.

written, respectively, as follows:

$$R = \frac{Z_{L\_R} Z_{L\_L0} Z_{L\_R0} A}{Z_{L\_R0}^2 + Z_{L\_R}^2 (A-1)} = \frac{Z_{L\_R0}^2}{\frac{Z_{L\_R0}^2}{Z_{L\_R}} + Z_{L\_R}(A-1)} \quad (15)$$

$$X = \frac{Z_{L\_L0}\sqrt{A-1}\left(Z_{L\_R}^2 - Z_{L\_R0}^2\right)}{Z_{L\_R0}^2 + Z_{L\_R}^2 (A-1)}. \quad (16)$$

However, as shown in Fig. 12, the series structure cannot intuitively describe the variation in impedance Z_L. Thus, the structure of resistance and reactance should be transferred from a series branch to a parallel branch, as shown in Fig. 12.

Thus, the relationship between different structures of impedance Z_L can be represented as

$$R + jX = \frac{R_1 jX_1}{R_1 + jX_1} = \frac{R_1 X_1^2}{R_1^2 + X_1^2} + j\frac{R_1^2 X_1}{R_1^2 + X_1^2}. \quad (17)$$

Then, according to (17), the transferred resistance and reactance in the parallel structure can be obtained as

$$\begin{cases} R_1 = R + \frac{X^2}{R} \\ X_1 = X + \frac{R^2}{X} \end{cases}. \quad (18)$$

Fig. 13 shows the resistance and reactance curves of T-type matching network ($k = 1$) and L-type matching network. It can be seen that with increasing Z_R, the resistance Z_{T_L} steadily decreases, which is consistent with (13). From the curve of the parallel resistance R_1 of the L-type case, it can be seen that the resistance variation range is much smaller than the variation range of the T-type case. Also with increasing Z_R, a minimum value exists in the curve of R_1. From (16), it can

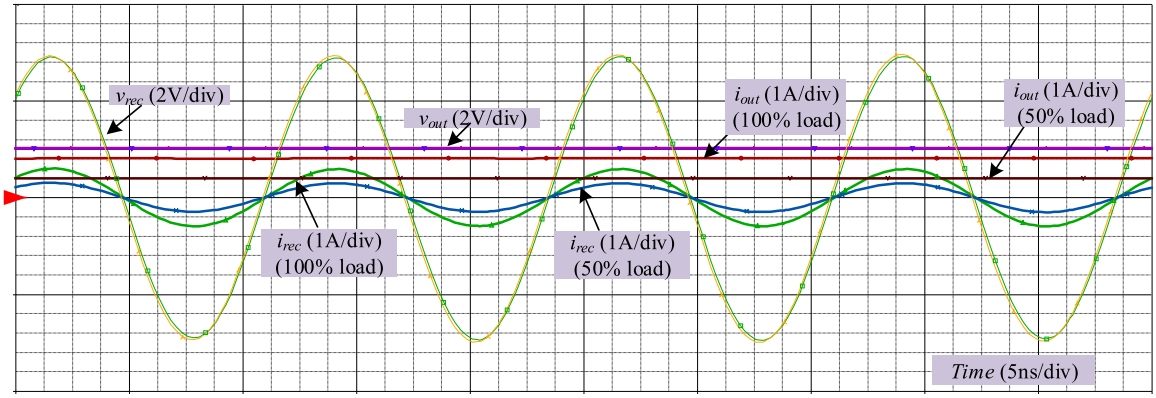

Fig. 17. Main current and voltage waveforms in 100% and 50% load conditions.

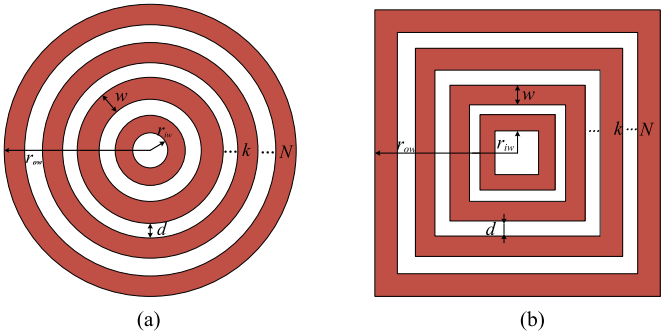

Fig. 18. Simplified winding structures of planar circular spirals and planar square spirals. (a) Circular spiral windings, (b) square spiral windings.

TABLE II
INDUCTANCES BASED ON DIFFERENT DESIGN METHODS ($d = 0.5$ MM, $r_{iw} = 1$ mm, $n = 4$)

Width (mil)	L_1 (nH) (This Paper Method)	L_2 (nH) (Current Sheet Method)	L_3(nH) (FEA Simulation)	L_1/L_2 (%)
10	58.14	70	87.19	83
15	61.19	74	89.32	82
20	64.73	79	92.31	82
25	68.56	84	96.51	82
30	72.55	89	101.57	82
35	76.67	94	105.99	82
40	80.88	100	108.87	81
45	85.14	105	114.03	81

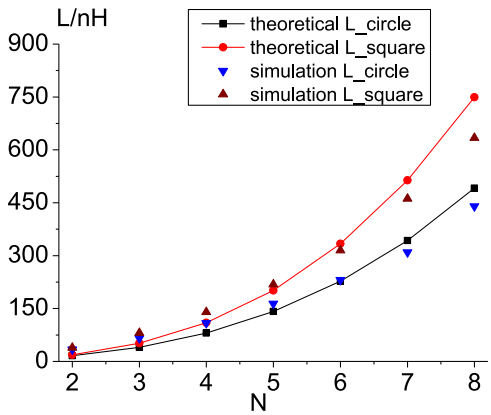

Fig. 19. Inductance curves of square and circular windings by calculation and simulation ($w = 1$ mm, $d = 0.5$ mm, $r_{iw} = 1$ mm).

be seen that when Z_{L_R} is larger than Z_{L_R0}, the reactance is larger than zero. This means the impedance is inductive, so the equivalent inductance of X_1 can be calculated by $L_1 = X_1/\omega$. Fig. 13 also shows that the inductance continues to decrease with increasing impedance Z_R. The small inductance will cause a great change in the inductive component in the resonant tank. Thus, the resonant frequency will also be greatly affected as analyzed in Section II.

To further investigate the effect of the impedance amplitude, a simplified inverter stage is adopted to be simulated. Fig. 14 shows the simplified circuit of the inverter stage with only load Z_L. Fig. 15 shows the simulation results of the switch drain-source voltages with different amplitudes of Z_L.

It can be seen that when $Z_L = 5\,\Omega$, the switch can turn on in ZVS condition, which operates at the desired point. When the impedance Z_L is larger than the desired value, the switch drain-source voltage reaches zero earlier than the original rising edge of the gate voltage. In addition, the peak switch voltage also increases in this condition. In contrast, when the impedance Z_L is smaller than the desired value, the switch drain-source voltage does not resonate to zero when the driving signal comes. On the basis of previous analysis, the increment of Z_R causes a decrease in transferred impedance Z_L in both L-type and T-type matching networks. However, in the L-type case, comparing the results of Fig. 5 and Fig. 15, it can be seen that the switch voltage trends are opposite. This means that the impedance phase dominates the change in switch drain-source voltage. Meanwhile, for the T-type matching network, the trends in Figs. 9 and 15 are the same.

From these analysis results, it can be concluded that the amplitude of impedance Z_L indeed affects the switch drain-source voltage and operating condition. However, the most important influencing factor is the impedance phase. The phase changes lead additional inductive or capacitive components into the

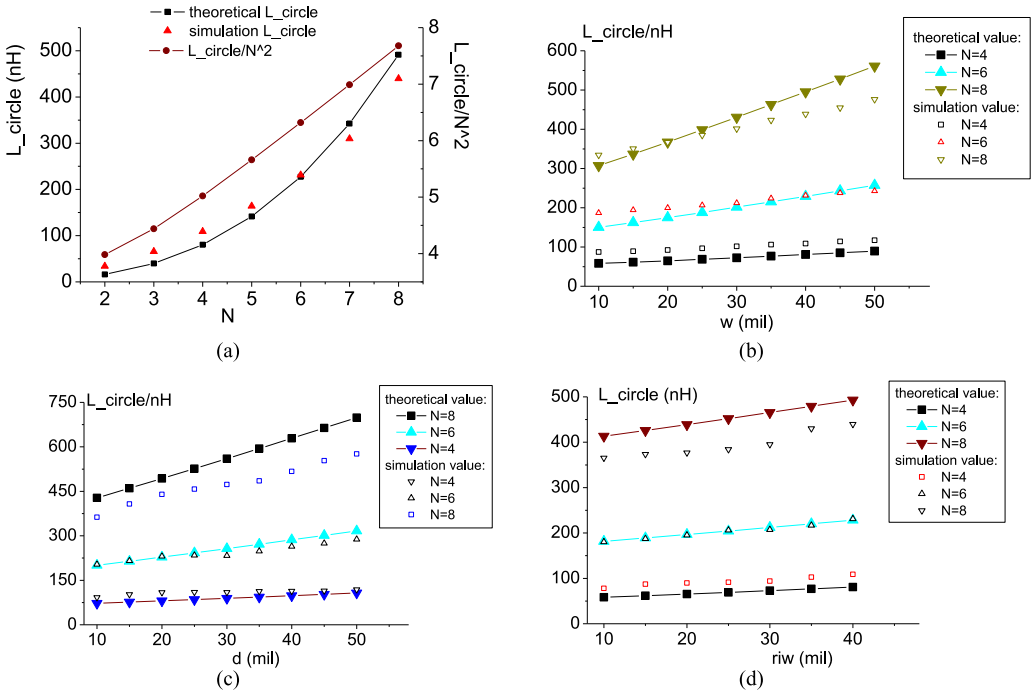

Fig. 20. Inductance curves at different winding parameters. (a) $w = 1$ mm, $d = 0.5$ mm, $r_{iw} = 1$ mm, (b) $d = 0.5$ mm, $r_{iw} = 1$ mm, (c) $w = 1$ mm, $r_{iw} = 1$ mm, (d) $w = 1$ mm, $d = 0.5$ mm

resonant tank, which causes the variation in inverter resonant frequency.

It is difficult to intuitively explain the amplitude effect of impedance Z_L. Here, the numerical analysis method can also be adopted to help analyze the simplified inverter stage. When the switch is turned off, the drain-source voltage $v_{\rm DS}$ should satisfy the following relationship based on KVL and KCL:

$$L_F C_F \frac{d^2 v_{\rm DS}(t)}{dt^2} + \frac{L_F}{Z_L}\frac{dv_{\rm DS}(t)}{dt} + v_{\rm DS}(t) = V_{\rm in}. \qquad (19)$$

By solving the difference equation, the switch drain-source voltage can be represented as

$$v_{\rm DS}(t) = \begin{cases} 0 & \text{(switch on)} \\ A_1 e^{-\alpha_1 t} + A_2 e^{-\alpha_2 t} + B & \text{(switch off)} \end{cases} \qquad (20)$$

where α_1 and α_2 are the characteristic roots of (19). Also, A_1, A_2, and B can be calculated according to system operating modes. Based on (20), the drain-source curves with different impedance Z_L can be obtained, similar to those shown in Fig. 15. From these results, the amplitude variation of impedance Z_L indeed affects the operating mode. However, the small amplitude changes will not introduce too much impact as shown in Fig. 9. Thus, it is quite effective to adopt the T-type matching network with resistive transferring property.

B. Phase Property of Rectifier Equivalent Impedance $Z_{\rm R}$

Meanwhile, in the earlier analysis, with the change in dc-load resistance, the rectifier equivalent impedance Z_R is always assumed to be resistive. The phase property of impedance Z_R should be investigated with the variation in dc output load. The

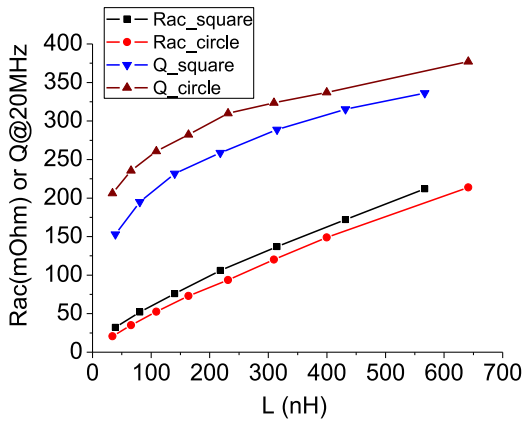

Fig. 21. Curves of ac resistance and quality factor for circular and square windings ($w = 1$ mm, $d = 0.5$ mm, $r_{iw} = 1$ mm).

circuit of the resonant rectifier adopted in the high-frequency dc/dc converter is shown in Fig. 16.

In [20], the corresponding equations and design method of the class E resonant rectifier are introduced in detail. On the basis of the analysis, the parameters of the resonant rectifier in the nominal output power condition can be optimally designed to achieve a resistive equivalent impedance Z_R. Under light-load conditions, with the help of Pspice software, the high-frequency circuit can be simulated. The phase of the impedance Z_R can be extracted from the fundamental component of rectifier input current and input voltage. Fig. 17 shows the main current and voltage waveforms of the rectifier in 100% and 50% load conditions. It can be seen that the dc output voltage and rectifier

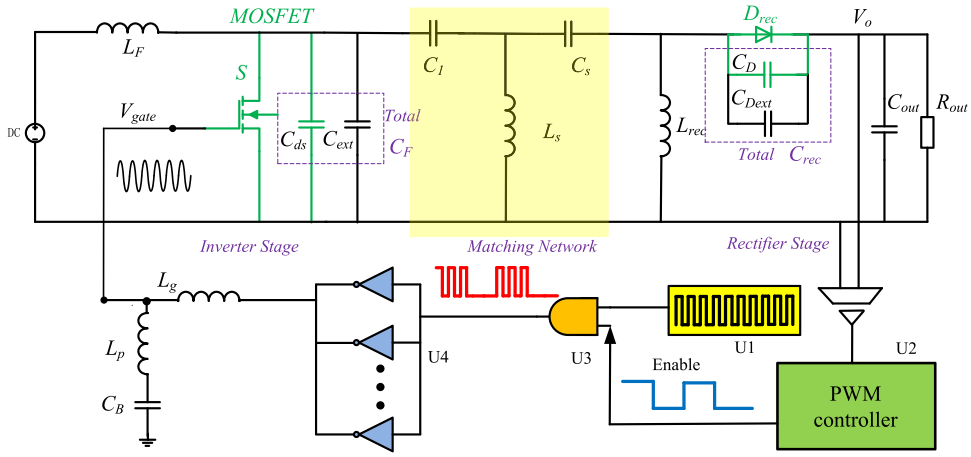

Fig. 22. Prototype circuit of 20 MHz high-frequency converter with the T-type matching network.

TABLE III
MAIN PARAMETERS AND DEVICE TYPES OF THE HIGH-FREQUENCY SYSTEM

Device Label	Value/Type	Device Label	Value/Type
L_F	22 nH	C_{out}	4 μF
S	SI7454	U_1	Oscillator LTC1799
C_{ext}	1470 pF	U_2	PWM controller/UC3842
C_1 C_s	1300 pF	U_3	AND Gate/NC7SZ08
L_s	47 nH	U_4	Inverter/NC7WZ04
L_{rec}	22 nH	L_g	110 nH
D_{rec}	STPS2H100A	L_p	72 nH
$C_{D\text{ext}}$	100 pF	C_B	0.1 μF

TABLE IV
PARAMETERS OF 47 NH HIGH-FREQUENCY INDUCTOR WITH DIFFERENT STRUCTURES

Structure	Discrete Inductor (1812SMS-47NGL)	Square Spiral PCB Inductor	Circular Spiral PCB Inductor
L/nH	47.1 (Coilcaft)	47.3	47.2
turns	6	4	4
R_{ac}@20 MHz/mΩ	65	57.1	46.5
Q@20 MHz	100	104.1	127.5
volume/mm^3	5 * 3.5 * 4	7 * 7 * 1.67	7 * 7 * 1.67

input voltage keep constant with the change of output power. The dc output current and rectifier input current varies with the change of output power. Meanwhile, with the variation of load, the fundamental components of rectifier input voltage and current are still almost in the same phase. So the impedance Z_R can be considered as resistive with the variation in dc output load.

IV. DESIGN OF HIGH-FREQUENCY SPIRAL INDUCTORS

In high-frequency condition, the inductances are within tens or hundreds of nanohenries; thus, planar spiral inductors can be used. Among them, planar square spirals and planar circular spirals are the two basic and widely used windings. Some effective equations and tools can help to design the planar spiral inductors with these typical structures [28]–[31]. A detailed design procedure is introduced in this paper, which can provide some guidance to design spiral inductors.

The simplified winding structures of the circular spiral inductors and square spiral inductors are shown in Fig. 18(a) and (b), respectively. Here, it starts from the planar circular spiral inductors. To further reduce the structure and ensure the inductance of the equivalent model is as close as possible to the inductance of the original structure, each circle can be equivalent to a quasi-regular octagon.

For the octagonal winding, the self-inductance of the planar circular spiral winding is the sum of that in the planar conductors. According to the self-inductance expression in [33], the total self-inductance of a planar circular spiral winding with N turns can be obtained. Also, the total mutual inductance is the sum of each mutual inductance that is inducted through the coupling between two conductors. For the mutual inductance calculation, only the mutual inductances between parallel conductors and the connected conductors with a certain angle are taken into consideration. The corresponding mutual inductances can be calculated based on [34]. Then the total inductance can be calculated. The inductance calculation method for square windings is similar to that for circular windings and is not described in detail here.

The inductances with different structure parameters, such as the width w, clearance distance d, turns N and inner radius r_{iw}, can be calculated based on the earlier method. Also, the three-dimensional (3-D) models corresponding to these structure parameters are established and simulated in the Ansoft Maxwell 3-D FEA software to verify the validity and feasibility of earlier analysis. From the inductance curves presented in Fig. 19, it can be seen that the calculated values of circular windings and square windings maintain good consistency with the simulation values. These results verify the correctness of the analysis.

Meanwhile, Table II compares the inductances designed with different methods, such as the current sheet method in [29] and FEA simulation. It can be seen that the trend is the same with the increment of width. The inductances of FEA simulation are larger than those of the former two methods. And, there is an

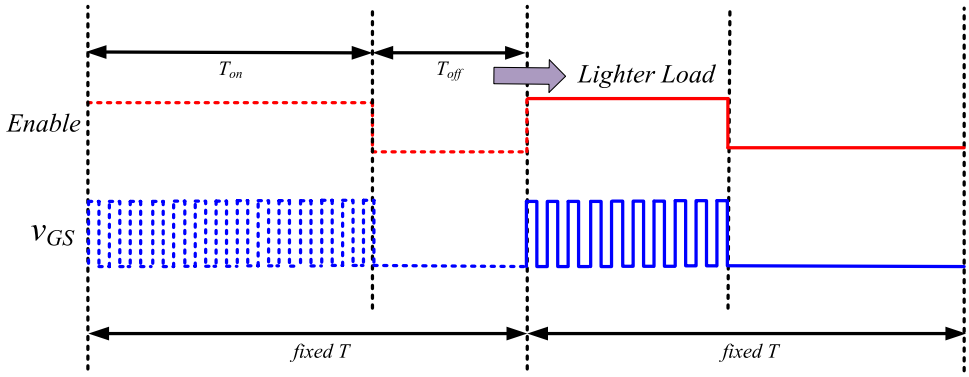

Fig. 23. Control diagram of the proposed high-frequency converter.

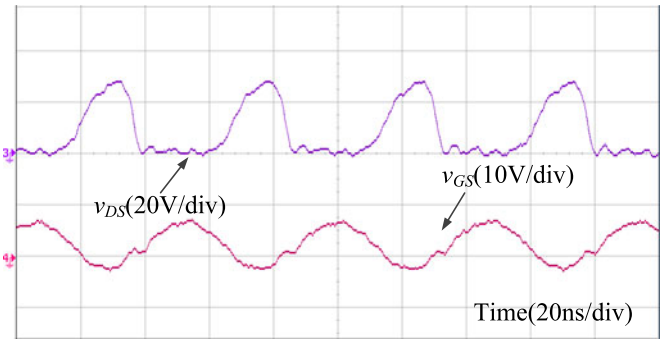

Fig. 24. Waveforms of switch and driving signal in full-load condition.

almost constant inductance ratio between the proposed method and the current sheet method. This shows that the method in this paper can be adopted to design spiral inductors.

Here, the circular winding structure is taken as an example to analyze the impact of the structure parameters as shown in Fig. 20. The winding turns N plays a remarkable role in determining its inductance values. As shown in Fig. 20(a), the ratio of inductance L and N^2 forms an approximately proportional relationship with N. From Fig. 20(b) to (d), it is seen that there is also a clear proportional relationship between inductance values and their width w, clearance d, and inner radius r_{iw}.

Meanwhile, for high-frequency inductors, a significant property is quality factor Q. When the frequency increases to tens of megahertz, because of the skin and proximity effects, the resistance increases rapidly. Higher Q means lower resistance at the same inductance value, which helps to reduce the conduction losses. In the dc condition, the resistances of square spiral inductors and circular spiral inductors can be calculated as

$$\begin{cases} R_{\text{square}} = \frac{8\rho}{h}\sum_{k=1}^{N}\frac{1}{\ln\left(\frac{r_{iw}+kw+(k-1)d}{r_{iw}+(k-1)w+(k-1)d}\right)} \\ R_{\text{circle}} = \frac{2\pi\rho}{h}\sum_{k=1}^{N}\frac{1}{\ln\left(\frac{r_{iw}+kw+(k-1)d}{r_{iw}+(k-1)w+(k-1)d}\right)} \end{cases}. \tag{21}$$

It can be seen that with same parameters, the dc resistance of square windings is almost 1.3 times larger than the dc resistance of circular windings. In high-frequency condition, the ac resistance forms an approximately proportional relationship with the dc resistance. Thus, the circular structure can reduce the winding resistance.

The same conclusion can be drawn from Fig. 21. Here, the circular winding structure always maintains a higher quality factor than the square winding structure. In future work, the winding resistance is expected to be further reduced in high-frequency condition. The preliminary idea is changing the copper width of different turns. For spiral inductors with variable width structure, the existing expressions cannot be adopted to design the inductors. However, they can be designed using the detailed method mentioned previously.

Based on aforementioned analysis, to design an inductor with a specific value, the turns can be first decided to make the inductance near the desired value. Then the width, clearance and inner radius can be slightly adjusted to realize the specific value. Meanwhile to reduce the winding resistance, it is better to adopt windings with wider track width.

V. Experimental Results

Based on the earlier analysis, a 20-MHz high-frequency resonant converter with the T-type matching network is designed and built in the laboratory. The circuit is shown in Fig. 22. The input voltage is 8 V, the output voltage is 5 V, and the output power is 10 W. The system component parameters are listed in Table III. In the prototype, the high-frequency capacitors are chosen from the 700-A series RF/microwave capacitors manufactured by ATC. The capacitor size is about 0.14 mm $\times$ 0.14 mm. As shown in Fig. 22, there are two input signals for the AND gate—one is the 20-MHz high-frequency signal generated by the oscillator, and the other is the pulsewidth-modulated (PWM) enable signal. Through the AND gate, the output signal is enhanced by several parallel CMOS inverters. Then, L_g, L_p, C_B, and switch input capacitor C_{iss} form a sinusoidal resonant gate driving network. The inductor can resonate with the switch input capacitor. Thus, part of the energy stored in the switch input capacitor can be saved in each period. However, in the conventional driving circuit, the energy of the input capacitor is completely dissipated in each period. Thus, the sinusoidal resonant driving method can greatly reduce the losses in the driving circuit. The losses of the sinusoidal resonant gate driver can be

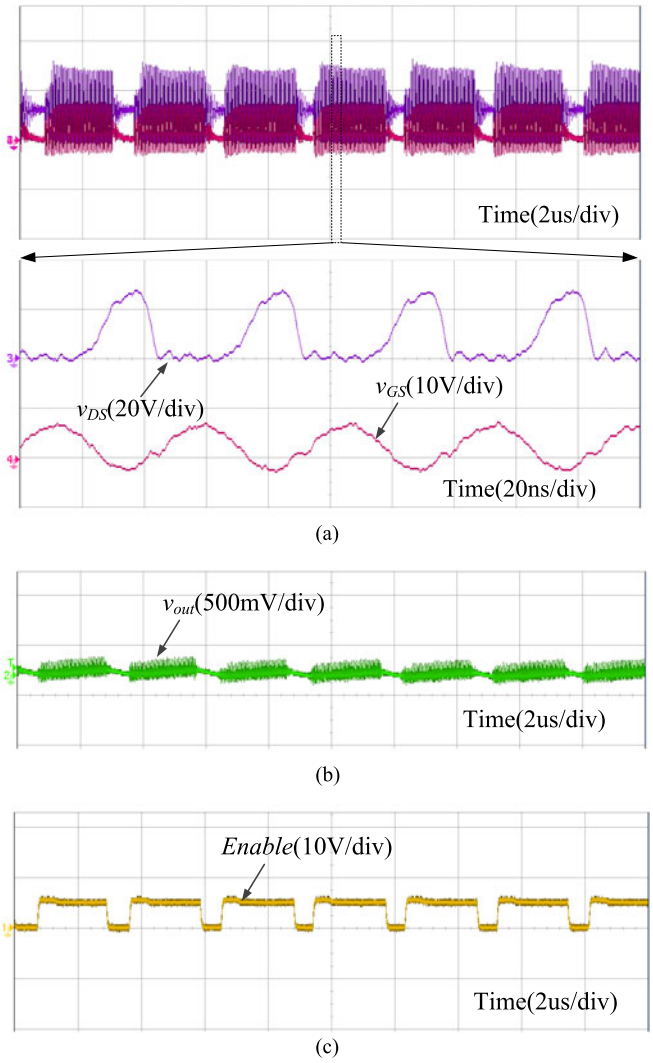

Fig. 25. Main voltage waveforms in 90% load condition. (a) Switch drain-source voltage and driving voltage, (b) output voltage (ac coupled), and (c) enable signal of the PWM controller

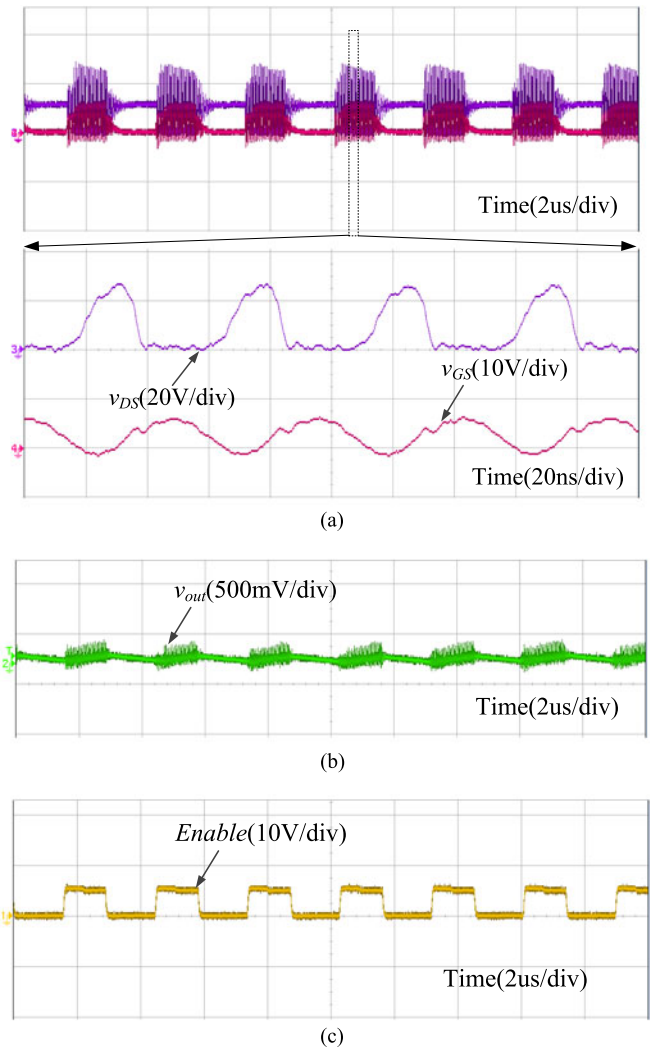

Fig. 26. Main voltage waveforms in 50% load condition. (a) Switch drain-source voltage and driving voltage, (b) output voltage (ac coupled), and (c) enable signal of the PWM controller

approximately calculated by

$$P_{\text{gate}} = 2R_g\pi^2 f^2 C_{\text{iss}}^2 V_{\text{gs}}^2. \tag{22}$$

where R_g represents the switch gate resistance, C_{iss} represents the switch input capacitance, and V_{gs} is the amplitude of the driving voltage.

Table IV shows the parameters of the 47-nH high-frequency inductor with different structures. According to the detailed analysis in Section IV, the spiral inductors with square and circular windings are designed. It can be seen that with a similar inductance, the circular spiral inductor has the smallest ac resistance and the highest quality factor, which can reduce the inductor losses and improve system efficiency. The effective thickness of the spiral inductor is calculated by the sum of the thickness of the PCB and copper trace.

The on-off control method is adopted to regulate the output voltage as shown in Fig. 23. It can be seen that the duty cycle of the enable signal changes with the variation in load in order to regulate the output voltage. Here, the chip UC3842 is chosen as the PWM controller, and the constant operating frequency can be set by adjusting the oscillation resistor and capacitor.

Fig. 24 shows the waveforms of the switch and driving signal under full load condition. It can be seen that the switch turns on in ZVS condition, and the driving signal is in sinusoidal form which can reduce the driving losses.

Figs. 25 and 26 show the control and switching voltage waveforms in the 90% and 50% load conditions, respectively. It can be seen that with the proposed resistive matching network, the switch can keep turning on in the ZVS condition within a wide load variation range. And, the duty cycle of the enable signal decreases with the reduction of load. Here, the frequency is set to 340 kHz.

Figs. 27 and 28 show the switch and driving signal voltage waveforms during the turn-on and turn-off transitions, respectively. It can be seen that because there is no bulk inductor in the proposed high-frequency converter, the transition time is short, and it can achieve very fast dynamic response.

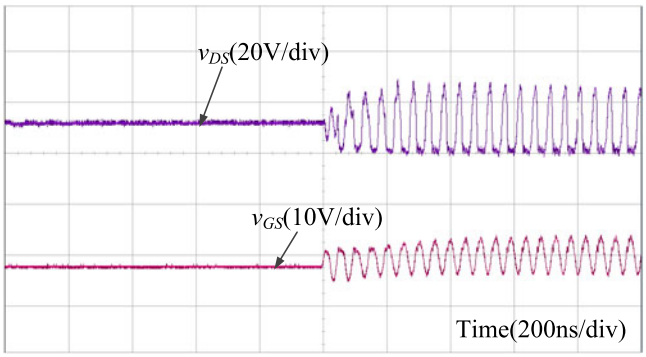

Fig. 27. Switch and driving signal waveforms during the turn-on transition.

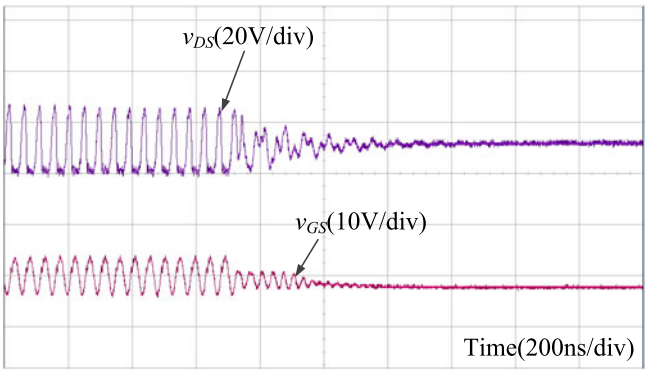

Fig. 28. Switch and driving signal waveforms during the turn-off transition.

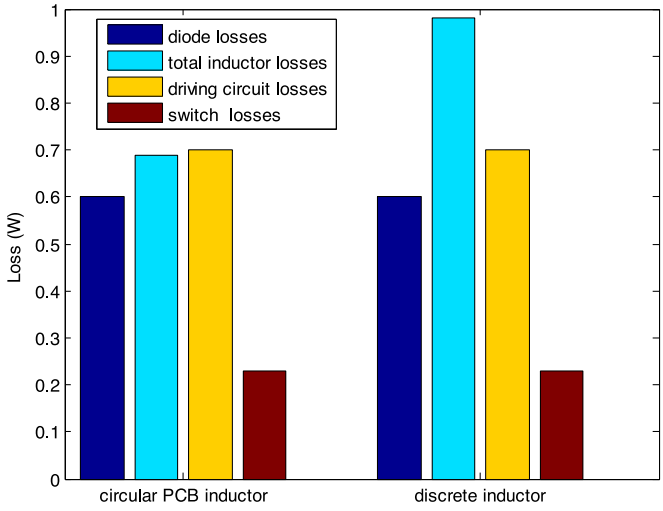

Fig. 29. Losses dissipation of high-frequency converter with circular PCB inductor and discrete inductor.

Fig. 29 shows the losses dissipation of high-frequency converter based on discrete solenoid inductors and spiral circular inductors. It can be seen that with a high quality factor, the losses of circular spiral inductor are lower than that of the discrete solenoid inductor, which helps to achieve high system efficiency. At the rated output power, the efficiency of the high-frequency converter can be improved from 79.9% to 81.8% when replacing the discrete solenoid inductors with circular spiral inductors.

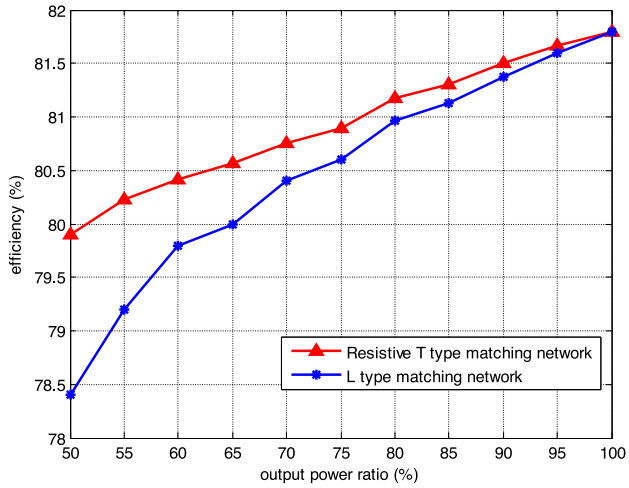

Fig. 30. Efficiency curves of high-frequency converter with different matching networks.

The loss model of the dc/dc converter can be approximately obtained from the following equations. The losses of the high-frequency capacitor with high quality factor are ignored. The losses of the inductor can be calculated as

$$P_L = I_{\text{ac,rms}}^2 \cdot R_{\text{ac}}. \tag{23}$$

For the soft-switching characteristics, the conduction losses of the switch can be calculated as

$$P_S = I_{\text{rms}}^2 \cdot R_{\text{DS, on}}. \tag{24}$$

The diode losses can obtained from (25), the losses can also be calculated according to the expression in the diode datasheet

$$P_D = I_F \cdot V_F. \tag{25}$$

In the driving circuit, besides the gate resistance losses in (22), the losses of the parallel CMOS inverters can be calculated as

$$P_{\text{inv}} = n \cdot C_{PD} \cdot V^2 \cdot f \tag{26}$$

where n is the number of the paralleled inverters, C_{PD} is the power dissipation capacitance, and V is the supply voltage.

Fig. 30 shows the efficiency curves in different prototype conditions. Comparing the efficiency curve of high-frequency converter with the resistive T-type converter and L-type converter, it can be seen that in the full load condition, their efficiencies are approximately the same. However, with decreasing output power, the high-frequency converter with T-type matching network is more efficient because of the good soft-switching characteristics in light-load condition. Besides the prototype in this paper, the π-type matching network and T-type matching network can also be adopted in other dc–dc/dc–ac high-frequency topologies to improve their performance.

The picture of the prototype is shown in Fig. 31. For the prototype, the total volume, including the driving stage and the control stage, is 0.19 in^3. For the power stage, the power density is approximately 150 W/in^3. Meanwhile, with increasing system output power, the system power density can be further improved. In 20 W output condition, the power density of the power stage can achieve 300 W/in^3.

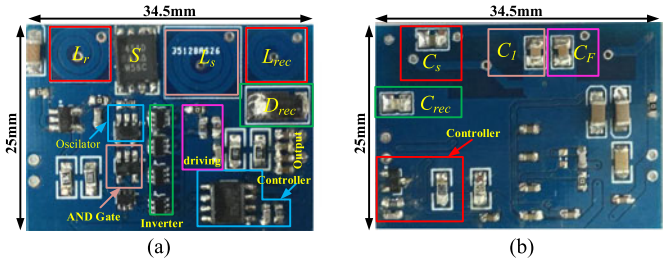

Fig. 31. Prototype. (a) Top view, and (b) bottom view.

For planar spiral inductors, the magnetic field will be vertical to the PCB. If a ground plane is placed under the spiral inductor, eddy currents at 20 MHz could cause extra losses, especially for higher power applications. Thus, in the prototype, this layout way is avoided. Also, in high-frequency condition, because the coupled effect of the magnetic field is not very clear, the inductors are not overlapped. The planar spiral inductor is easy to be integrated. In the future work, with the integration technology, the volume of the driving stage and control stage can be significantly reduced and system power density can be further improved.

VI. Conclusion

This paper proposes and investigates two resistive matching networks for high-frequency resonant converters. The T-type matching network and π-type matching network can maintain resistive transferring characteristics with proper design, which can guarantee the switch operating in a good switching mode within wide load variation range. In addition, a detailed analysis of planar spiral inductor is conducted. Also, the quality factor characteristics of different winding structures are analyzed. A 20-MHz prototype with the resistive T matching network validates the feasibility of the proposed converter and design methods. The system efficiency is significantly improved in light-load condition.

References

[1] D. J. Perreault *et al.*, "Opportunities and challenges in very high frequency power conversion," in *Proc. IEEE APEC.*, 2009, pp. 1–14.

[2] J. M. Rivas, D. J. Jackson, O. Leitermann, A. D. Sagneri, Y. Han, and D. J. Perreault, "Design consideration for very high frequency DC–DC converters," in *Proc. IEEE APEC.*, 2013, pp. 835–839.

[3] A. Knott *et al.*, "Evolution of very high frequency power supplies," *IEEE J. Emerg. Sel. Topics Power Electron.*, vol. 2, no. 3, pp. 386–394, Sep. 2014.

[4] J. S. Glaser and J. M. Rivas, "A 500 W push–pull DC–DC power converter with a 30 MHz switching frequency," in *Proc. IEEE APEC.*, 2010, pp. 654–661.

[5] Y. Guan, Y. Wang, W. Wang, and D. Xu, "A high frequency CLCL converter based on leakage inductance and variable width winding planar magnetics," *IEEE Trans. Ind. Electron.*, vol. PP, no. 99, pp. 1–1, doi: 10.1109/TIE.2017.2716878.

[6] J. M. Rivas, R. S. Wahby, J. S. Shafran, and D. J. Perreault, "New architectures for radio-frequency DC–DC power conversion," *IEEE Trans. Power Electron.*, vol. 21, no. 2, pp. 380–393, Mar. 2006.

[7] M. P. Madsen, A. Knott, and M. A. E. Andersen, "Very high frequency resonant DC/DC converters for LED lighting," in *Proc. Appl. Power Electron. Conf. Expo.*, 2013, pp. 835–839.

[8] W. Liang *et al.*, "Low mass RF power inverter for Cubesat plasma thruster using 3D printed inductors," in *Proc. Workshop Control Modeling Power Electron.*, 2016, pp. 1–7.

[9] Y. Guan, Y. Wang, D. G. Xu, and W. Wang, "A 1 MHz half-bridge resonant DC/DC converter based on GaN FETs and planar magnetics," *IEEE Trans Power Electron.*, vol. 32, no. 4, pp. 2876–2891, Apr. 2017.

[10] Y. Guan, Y. Wang, Q. Bian, X. Hu, W. Wang, and D. Xu, "High Efficiency Self-Driven Circuit with Parallel Branch for High Frequency Converters," *IEEE Trans. Power Electron.*, vol. PP, no. 99, pp. 1–1, Jul. 1990.

[11] Y. Guan, Y. Wang, Q. Bian, X. Hu, W. Wang, and D. Xu, "High efficiency self-driven circuit with parallel branch for high frequency converters," *IEEE Trans. Power Electron.*, doi: 10.1109/ TPEL.2017.2724545.

[12] M. M. Jovanovic, "Merits and limitations of resonant and soft-switched converters," in *Proc. Telecommun. Energy Conf.*, 1992, pp. 51–58.

[13] Y. Guan, Y. Wang, W. Wang, and D. Xu, "Analysis and design of high frequency DC/DC converter based on resonant rectifier," *IEEE Trans. Ind. Electron.*, vol. PP, no. 99, pp. 1–1. doi: 10.1109/TIE.2017.2698412.

[14] J. Warren, K. Rosowski, and D. Perreault, "Transistor selection and design of a VHF DC–DC power converter," *IEEE Trans. Power Electron.*, vol. 23, no. 1, pp. 27–37, Jan. 2008.

[15] J. M. Burkhart, R. Korsunsky, and D. J. Perreault, "Design methodology for a very high frequency resonant boost converter," *IEEE Trans. Power Electron.*, vol. 28, no. 4, pp. 1929–1937, Apr. 2013.

[16] J. M. Rivas, Y. Han, O. Leitermann, A. D. Sagneri, and D. J. Perreault, "A high-frequency resonant inverter topology with low-voltage stress," *IEEE Trans. Power Electron.*, vol. 23, no. 4, pp. 1759–1771, Jul. 2008.

[17] J. M. Rivas, O. Leitermann, Y. Han, and D. J. Perreault, "A very high frequency DC–DC converter based on a class Φ2 resonant inverter," *IEEE Trans. Power Electron.*, vol. 26, no. 10, pp. 2980–2992, Oct. 2011.

[18] L. Raymond, W. Liang, J. Choi, and J. Rivas, "27.12 MHz large voltage gain resonant converter with low voltage stress," in *Proc. IEEE ECCE.*, 2013, pp. 1814–1821.

[19] L. C. Raymond, W. Liang, and J. M. Rivas-Davila, "Performance evaluation of diodes in 27.12MHz Class-D resonant rectifiers under high voltage and high slew rate conditions," in *Proc. Workshop Control Modeling Power Electron.*, 2014, pp. 1–9.

[20] J. A. Santiago-Gonzalez, K. M. Elbaggari, K. K. Afridi, and D. J. Perreault, "Design of class E resonant rectifiers and diode evaluation for VHF power conversion," *IEEE Trans. Power Electron.*, vol. 30, no. 9, pp. 4960–4972, Sep. 2015.

[21] Y. Han, O. Leitermann, D. A. Jackson, J. M. Rivas, and D. J. Perreault, "Resistance compression networks for radio-frequency power conversion," *IEEE Trans. Power Electron.*, vol. 22, no. 1, pp. 41–53, Jan. 2007.

[22] R. Pilawa-Podgurski, A. D. Sagneri, J. M. Rivas, D. I. Aderson, and D. J. Perreault, "Very high frequency resonant boost converter," *IEEE Trans. Power Electron.*, vol. 24, no. 6, pp. 1654–1665, Jun. 2009.

[23] J. Hu, A. D. Sagneri, J. M. Rivas, Y. Han, S. M. Davis, and D. J. Perreault, "High-frequency resonant SEPIC converter with wide input and output voltage ranges," *IEEE Trans. Power Electron.*, vol. 27, no. 1, pp. 189–200, Jan. 2012.

[24] Coilcraft, Midi Spring Air Core Inductors. (2015). [Online]. Available: http://www.coilcraft.com/pdfs/midi.pdf

[25] W. Liang, J. Glaser, and J. Rivas, "13.56 MHz high density DC-DC converter with PCB inductors," in *Proc. IEEE APEC.*, pp. 633–640, 2013.

[26] A. D. Sagneri, D. I. Anderson, and D. J. Perreault, "Transformer synthesis for VHF converters," in *Proc. IEEE IPEC*, 2010, pp. 2347–2353.

[27] J. Hu, "Design of a low-voltage low-power dc–dc HF converter," M.S. thesis, Dept. Elect. Eng. Comput. Sci., Mass. Inst. Technol., Cambridge, MA, USA, 2008.

[28] F. E. Terman, *Radio Engineer's Handbook*. New York, NY, USA/London, UK: McGraw-Hill, 1943.

[29] 2017. [Online]. Available: http://www.tesla-institute.com/!app/sim/slpscic.php

[30] H. A. Wheeler, "Simple inductance formulas for radio coils," *Proc. Inst. Radio Eng.*, vol. 16, no. 10, pp. 1398–1400, Oct. 1928.

[31] S. S. Mohan, M. del Mar Hershenson, S. P. Boyd, and T. H. Lee, "Simple accurate expressions for planar spiral inductances," *IEEE J. Solid-State Circuits*, vol. 34, no. 10, pp. 1419–1424, Oct 1999.

[32] L. Gu, W. Liang, L. C. Raymond, and J. Rivas-Davila, "27.12MHz GaN Bi-directional resonant power converter," in *Proc. 2015 IEEE 16th Workshop Control Modeling Power Electron.,* Vancouver, BC, Canada, 2015, pp. 1–7.

[33] F. W. Grover, *Inductance Calculations*. Princeton, NJ, USA: Van Nostrand, 1946 (reprinted by, New York, NY, USA: Dover, 1962).

[34] H. M. Greenhouse, "Design of planar rectangular microelectronic inductors," *IEEE Trans. Parts, Hybrids, Packag.*, vol. PHP-10, no. 2, pp. 101–109, Jun. 1974.

Yueshi Guan (S'15) was born in Heilongjiang Province, China, in 1990. He received the B.S. degree and the M.S. degree in electrical engineering in 2013 and 2015, respectively, from Harbin Institute of Technology, Harbin, China, where he is currently working toward the Ph.D. degree.

His current research interests include in the areas of high-frequency and very high-frequency converters, single-stage ac/dc converter, and LED lighting systems.

Qing Bian was born in Jiangsu Province, China, in 1993. She received the B.S. degree in electrical engineering in 2016 from Harbin Institute of Technology, Harbin, China, where she is currently working toward the M.S. degree in electrical engineering.

Her current research interests include high-frequency converters and high-step-up dc/dc converters.

Yijie Wang (S'09–M'15–SM'15) was born in Heilongjiang Province, China, in 1982. He received the B.S., M.S., and Ph.D. degrees in electrical engineering from Harbin Institute of Technology, Harbin, China, in 2005, 2007, and 2012, respectively.

From 2012 to 2014, he was a Lecturer with the Department of Electrical and Electronics Engineering, Harbin Institute of Technology, where since 2015, he has been an Associate Professor. His current research interests include dc–dc converters, soft-switching power converters, power factor correction circuits, digital control electronic ballasts, and LED lighting systems.

Xihong Hu was born in Hubei Province, China, in 1994. He received the B.S. degree in electrical engineering in 2017 from Harbin Institute of Technology, Harbin, China, where he is currently working toward the M.S. degree in electrical engineering.

His current research interests include topologies and magnetics design of high-frequency converters.

Bin Liu was born in Heilongjiang Province, China, in 1990. He received the B.S. degree in electrical engineering from China University of Mining and Technology, Jiangsu, China, in 2015, and the M.S. degree in electrical engineering from Harbin Institute of Technology, Harbin, China, in 2017.

His current research interests include topologies and driving strategies of high-frequency converters.

Wei Wang was born in Heilongjiang, China, in 1963. She received the B.S. degree in automatic test and control, the M.S. degree in electrical engineering, and the Ph.D. degree in mechanical electronic engineering from Harbin Institute of Technology, Harbin, China, in 1984, 1990, and 2002, respectively.

Since 2003, she has been a Professor with the Department of Electrical Engineering, Harbin Institute of Technology. She is currently engaged in research on soft-switching converters, digital control electronic ballast, and regenerative energy converter technique.

Dianguo Xu (M'97–SM'12–F'17) was born in Heilongjiang, China, in 1960. He received the B.S. degree in control engineering from Harbin Engineering University, Harbin, China, in 1982, and the M.S. and Ph.D. degrees in electrical engineering from Harbin Institute of Technology (HIT), Harbin, in 1984 and 1989, respectively.

In 1984, he joined the Department of Electrical Engineering, HIT, as an Assistant Professor, where since 1994, he has been a Professor. He was the Dean of School of Electrical Engineering and Automation, HIT, from 2000 to 2010. He is now the vice president of HIT. His current research interests include renewable energy generation technology, power quality mitigation, sensorless vector-controlled motor drives, high-performance servo system. He has authored or coauthored over 600 technical papers.

Dr. Xu is an Associate Editor of the IEEE TRANSACTIONS ON INDUSTRIAL ELECTRONICS and the IEEE JOURNAL OF EMERGING AND SELECTED TOPICS IN POWER ELECTRONICS. He is the Chairman of the IEEE Harbin Section.